Passive control of a planar offset attaching jet using a perforated bottom plate over a closed cavity

Yu Xia*
School of Aeronautics and Astronautics, Dalian University of Technology, Dalian, Liaoning 116024, China

Nan Gao†
Institute for Turbulence-Noise-Vibration Interaction and Control, Harbin Institute of Technology, Shenzhen, Guangdong 518055, China

Dan Ewing
Department of Mechanical Engineering, McMaster University, Hamilton, Ontario, Canada L8S 4L8

(Received 8 August 2019; accepted 17 April 2020; published 18 May 2020)

The effects of a perforated bottom wall on the unsteadiness of a turbulent offset attaching jet are experimentally investigated for a jet with a Reynolds number of 14 600 initially offset one jet height. The effects of two independent control parameters, the open area of the perforated wall and the depth of the air cavity underneath the wall, are considered. Two distinct flow patterns are observed. In the first, when either the open area or the cavity depth is small, the recirculating flow is largely above the perforated plate and there is only slight change in the jet trajectory. In the second, when the open area and the cavity depth are both large, the perforated plate and cavity serve as a channel for flow to recirculate upstream with a large amount of flow penetrating the perforated plate in the reattachment region, traveling upstream in the cavity, and flowing into the recirculation bubble near the jet exit. Jet trajectories become much more parallel to the wall. The flow patterns can be distinguished from the change in the base static pressure and the jet curvature. In both flow patterns, the lower-frequency motion becomes much more in phase in the spanwise direction due to the attenuation of the spanwise varying disturbances.

DOI: 10.1103/PhysRevFluids.5.054603

I. INTRODUCTION

Boundary layer separations and reattachments can be found in various applications and have been studied extensively. The characteristics of a separated shear layer in flows over a backward facing step, a bluff body, or an airfoil were reviewed by Simpson [1] and Chen *et al.* [2]. There are several unsteady modes found in these flows. There is a shear layer mode or rolling up of the large-scale structures due to Kelvin-Helmholtz instability in the initial part of the shear layer [1,3]. The shear layer structures amalgamate while evolving, causing the characteristic frequency of the structures to decrease before reattachment to the bottom wall [3–7]. There is a shedding mode [8,9] that reflects the large-scale structures shed downstream from the recirculation region [10,11]. There is also evidence of lower-frequency flapping modes observed in flows over a backward facing

*Present address: Mechanical and Manufacturing Engineering, University of Melbourne, Victoria 3010, Australia.
†gaonan@dlut.edu.cn

 ©2020 American Physical Society

step [3,5,12], planar offset attaching jets [13,14], and other reattaching flows [15–17] causing low-frequency fluctuations of the reattachment point. The low-frequency fluctuations typically occur in two frequency ranges $\mathrm{St} = fH/U_\infty$ of 0.01–0.02 [5,12,14] and 0.05–0.07 [11,18], where H is the step height and U_∞ is the freestream velocity.

The cause of the flapping motion is not fully resolved, but a number of different possible causes have been proposed. Causes for the lower-frequency range include instantaneous imbalance of the mass into and out of the separation bubble [19], a quasiperiodic motion of the secondary separation bubble [12], feedback from the attaching and splitting of the shear layer structures [3], and upstream propagation of low-frequency disturbances [5,6], while those for the higher-frequency range include shedding [8] or flow oscillations [11]. Moreover, some features of the flapping motion are not clear. Eaton and Johnson [19] conjectured that the low-frequency flapping motion in a backward facing step flow with a modest Reynolds number was two dimensional, whereas Statnikov *et al.* [20] and Scharnowski *et al.* [21] reported that the low-frequency motion ($\mathrm{St} \approx 0.01$) in a subsonic backward facing step flow was a three-dimensional cross-pumping mode with a spanwise length scale of approximately $2H$. Stability analysis has shown evidence of a number of three-dimensional mechanisms including instability in the flow on the step face and the lifting of the shear layer [22–24].

The low-frequency flapping can result in a large dynamic load on structures under a reattaching flow and thus there have been a number of investigations on methods to mitigate these fluctuations, including active control methods using synthetic jet [25] or plasma actuators [26] and passive control methods such as a modified geometry [27]. Heenan and Morrison [5,6] replaced part of the bottom wall under a backward facing flow with a permeable surface. They found that the permeable wall significantly attenuated the low-frequency motion as well as the upstream propagation of low-frequency disturbances. Their findings provide a useful control method to alleviate the dynamic load and lead to their proposal that the flapping motion was caused directly by the upstream propagating disturbances. There were a number of aspects that Heenan and Morrison [5,6] did not consider. These include why and how the upstream propagating disturbances were prohibited by the perforated plate and the role of the cavity depth in damping the low-frequency modes. Moreover, the effect that the permeable plate has on the three-dimensionality of the unsteady motion was not studied.

The objective here is to examine the effect of the perforated bottom plate on the development of low-frequency motion in a reattaching jet flow formed when a planar jet issued parallel to a solid wall offset from the jet exit. Shear layers form along the lower and upper sides of the jet [28], but when the offset distance is sufficiently small the inner layer tends to interact with the wall before the flow is fully developed [13,14]. The flows show evidence of low-frequency motion in the recirculating region similar to other reattaching shear layer flows [14]. Characteristics of the recirculating flow over walls of different open-area ratios and cavity depths and their relations to the low-frequency motion are studied in detail in this investigation.

The development of offset jets with a Reynolds number of 14 600 and initial offsets of one jet height over a solid wall and perforated walls is characterized using particle image velocimetry (PIV) and measurements of base pressure fluctuations across the flow. Results show that a perforated wall, even one with the smallest open area and cavity depth, significantly increases the spanwise coherence of base pressure fluctuations. Only perforated plates with a combination of large open area and large cavity depth have a significant impact on the jet evolution in the streamwise direction. The experimental methodologies will be discussed in Sec. II, followed by the results in Sec. III, and a discussion and summary in Sec. IV.

II. EXPERIMENTAL METHODOLOGIES

The measurements were performed for a jet exiting a long channel as shown in Fig. 1(a), similar to that used by Gao and Ewing [13,14,29]. The rectangular channel made of cold rolled steel plates had a height H_j of 20 mm, a length of 1200 mm ($60H_j$), and a width of 300 mm ($15H_j$). The

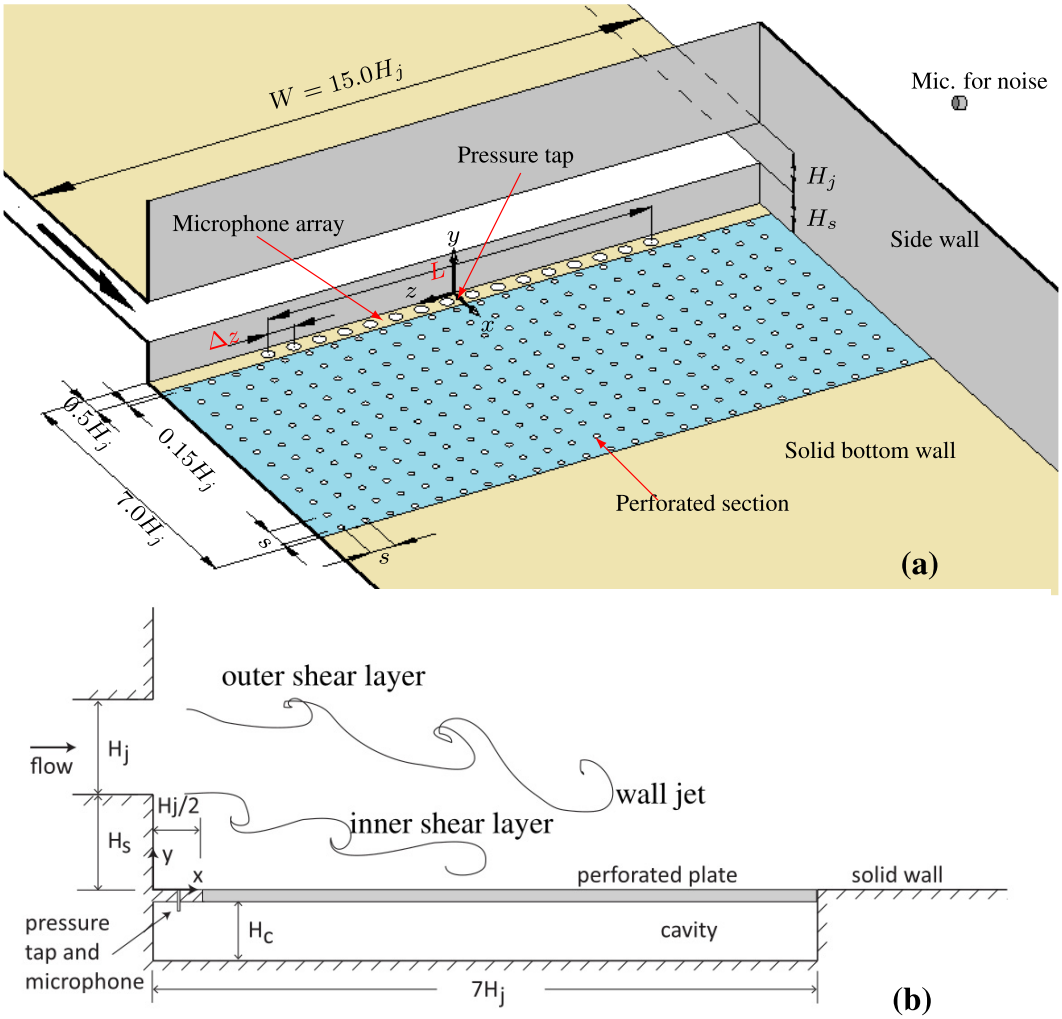

FIG. 1. Schematics of the facility in (a) a perspective view without the front sidewall and (b) a side view.

air flow to the channel from a blower was conditioned in a $0.6 \times 0.6 \times 0.6$ m^3 settling chamber with flow straighteners inside. The flow from the channel developed over a 500-mm-long ($25H_j$), 300-mm-wide ($15H_j$) Plexiglas plate positioned parallel with the channel. The vertical distance from the lower edge of the channel to the plate was 20 mm ($H_s = H_j$), as shown in Fig. 1. Two side panels with a height of 170 mm were used to confine the jet.

The bottom wall included a removable section across the span (from $x/H_j = 0.5$ to 7.0) that could be replaced with perforated plates, as shown in Fig. 1. Four different perforated plates with a standard round straight pattern of 3-mm-diam d holes ($d/H_j = 0.15$) were used where the spacing between neighboring holes s was 11.8, 8.5, 5.8, and 4.2 mm, in both the streamwise and spanwise directions (s/d of 3.9, 2.8, 1.9, and 1.4). The corresponding open-area ratio γ was 0.05, 0.1, 0.2, and 0.4, respectively, in the region $x/H_j = 0.5$–7.0. The arrangement of the holes was symmetric about the centerline of facility ($z = 0$) and the streamwise position of the center of the first row was $x/H_j = 0.65$ in all perforated plates. There was an air-tight cavity located below the perforated plate at $0 \leqslant x/H_j \leqslant 7.0$ with a width that spanned the test section and a depth that could be varied and

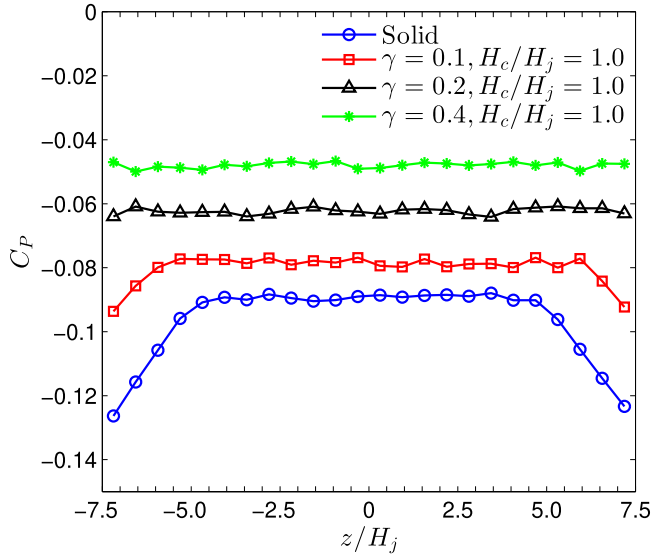

FIG. 2. Spanwise distributions of the static base pressure measured at $x/H_j = 0.05$ for Re = 14 600.

was set to $0.25H_j$, $0.5H_j$, $0.75H_j$, and $1.0H_j$ by adding solid plates into the cavity. Measurements of the mean static pressure across the flow (at $x/H_j \sim 0.05$) for the full depth cavity in Fig. 2 suggested that the flow was uniform in the spanwise direction in the central part of the flow.

The measurements were performed with an averaged jet velocity of $U_j = 11.6$ m/s, determined by integrating the velocity profiles measured at the exit. This corresponded to a Reynolds number $U_j H_j/\nu = 14\,600$. The development of the flow field on the centerline plane $z = 0$ was measured using a Lavision two-dimensional PIV system. Droplets of olive oil with a mean particle diameter of 1 μm were used as the tracer particles. The particles were injected into the inlet of the blower using an in-house droplet generator designed following that in [30]. A 200-mJ dual-head Nd:YAG Litron Nano pulse laser system was used to illuminate the tracer particles. The laser pulses were triggered at a rate of 25 Hz. A Highspeedstar camera with a 1024 × 1024 pixel resolution was used to capture the images. The separation time between two exposures was 100 μs to allow seed particles to travel 6 pixels based on the mean jet velocity. A total of 2000 image pairs (N_s) were collected for processing in each flow. The DAVIS 8.3 software package was used for image acquisition and postprocessing. Vectors were computed using the cross-correlation method with 50% overlap using a multipass approach with 32 × 32 and 16 × 16 pixel interrogation windows. This resulted in a spatial resolution of 2 mm ($0.1H_j$). The closest point to the wall was 2 mm ($0.1H_j$). The uncertainty of the PIV measurements was found to be less than 3% for a 95% confidence interval, following the procedure outlined by Wieneke [31]. Uncertainties of the reported Reynolds stresses due to the limited sample numbers were less than 3.2% of their values, evaluated using $\sqrt{2/N_s}$ [32], for a 95% confidence level.

The time-mean reattachment locations for the flow over the solid wall and the perforated wall with small open area or small cavities were evaluated using forward flow probability (FFP) as proposed by Spazzini *et al.* [12]. This was not effective in all cases so the development of the flows were also characterized by considering the curvature along a streamline approximately corresponding to the location of the local maxima in the mean velocity. The curvature was computed using a least-squares method following [33]. The streamwise position of minimum curvature was found to approximately correspond to the 50% FFP in the case with a solid bottom wall as discussed below.

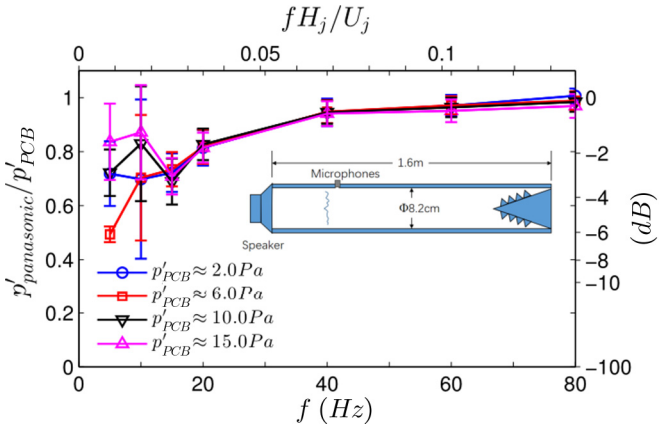

FIG. 3. Comparison of the responses (root mean square of the outputs) to sinusoidal pressure waves of different frequencies and amplitudes for the Panasonic WM60B microphones and a PCB 378B11 microphone, measured using a dynamic calibration rig shown in the inlay.

The static base pressure P on the wall for all the configurations was measured on the centerline of the facility at $x/H_j = 0.25$ using a pressure tap with an outer diameter of 1.2 mm and a pressure transducer that was calibrated using a water manometer with a resolution of 0.1 Pa. The uncertainties in the coefficients of the static wall pressure were within $\pm 2\%$ for a 95% confidence interval. The fluctuating base pressure p was measured at $x/H_j = 0.25$ using a spanwise array of 16 Panasonic WM-60B microphones. The microphones were mounted flush with the wall at locations in the range $-4.69 \leqslant z/H_j \leqslant 4.69$ or a total length L of 0.1875 m ($9.375H_j$) with a spacing $\Delta z/H_j = 0.625$. The microphones were calibrated *in situ* with a piston phone at 1000 Hz with an amplitude of 104 dB. The signals from the microphones were recorded using a PC with an NI-6014 data acquisition card and a Labview routine. The sampling frequency was 4096 Hz and sampling time was 180 s. The data were divided into 180 independent blocks of 1 s and the cross spectrum of the fluctuating pressure at z and z' was computed following [32]. The cross spectrum of fluctuating wall pressure between spanwise locations z and z' was computed as

$$F_{pp}(z, z', f) = \frac{1}{N_d T} \sum_{k=1}^{N_d} \hat{p}^{\star}(z, f, T)\hat{p}(z', f, T), \tag{1}$$

where $\hat{p}(z, f, T)$ is the Fourier transform for each block computed here using a Hanning Window, the star denotes the complex conjugate, f is the temporal frequency, T is the length of each data block (1 s), and the number of data blocks N_d is 180. Cross spectra where the spanwise separation $\delta z = z' - z$ were equal were averaged. The autospectrum F_{pp} where δz was zero was computed using this approach. The uncertainty in the magnitude of the individual spectra was less than $\pm 7.5\%$ for a 95% confidence interval [32]. The mean-square value of the fluctuating pressure $\overline{p^2}$ was obtained by integrating the pressure autospectrum. Kaiser window-based finite impulse response digital lowpass and bandpass filters were applied to the transient wall pressure to illustrate the contributions from different motions. The filtered pressure was denoted by $\tilde{p}$.

The microphones used here have an approximately flat response range from 20 to 20 000 Hz ($f^* = 0.035$–35.5). The low-frequency response (5–80 Hz) characterized using a dynamic calibration facility is shown in Fig. 3. The response to sinusoidal excitations was compared to that of a PCB microphone (378B11) that had a flat response (± 2 dB) to 3.5 Hz (± 1 dB to 7 Hz). The microphones sense the flow though pinholes 10 mm apart in the azimuthal direction. The average response (for five randomly selected microphones) indicates that the attenuation was 2 dB at 20 Hz ($f^* = 0.035$), as expected, and 3 dB at 15 Hz ($f^* = 0.026$). The attenuation at lower frequency ($f^* < 0.026$)

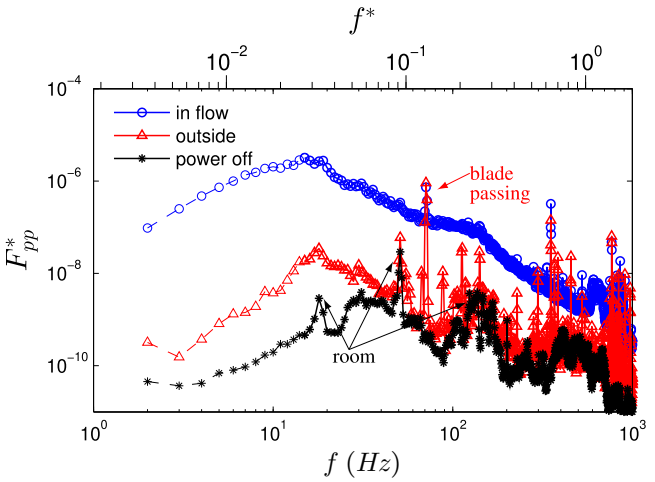

FIG. 4. Comparison of the pressure spectra measured at $x/H_j = 0.25$ and $z/H = 0.625$ (○) and outside the flow (facility) (△) for the flow over the solid wall and at $x/H_j = 0.25$ and $z/H = 0.625$ (∗) without flow.

was typically less than 6 dB, but showed more variation with pressure level and between sensors (indicated by the range bars in Fig. 3). Thus, the measurements below 15 Hz were considered unreliable and distinguished here by plotting the spectra in this range using dashed lines.

A microphone was positioned outside the flow to measure the ambient noise level for the case of the flow over the solid wall. A comparison of the spectra of the fluctuating pressure below and outside the flow is shown in Fig. 4. Results measured without the facility operating are also shown. The results show evidence of spikes associated with the operation of the fan most notable at 70 Hz that is evident in the measure spectra. There is evidence of peaks at 18, 51, and 113 Hz that appear associated with the room. These peaks appear small relative to the measurements below the flow, as evident when they are compared on the later linear spectra.

III. RESULTS

A. Time-mean flow field

The development of the flow over the solid bottom wall is shown in Fig. 5 using streamlines computed from the measured mean velocities. The planar jet curved toward the wall from the exit and attached to the wall before turning parallel to the wall. The recirculation region formed between the jet and the wall was characterized using the forward flow probability in Fig. 5. The forward

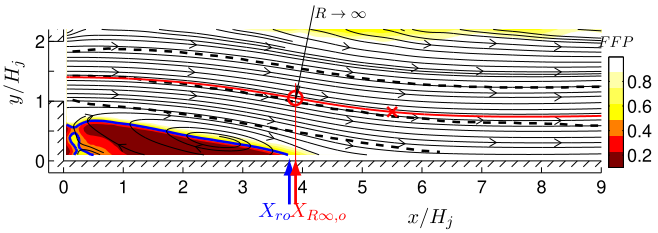

FIG. 5. Mean streamlines of the flow over the solid wall with contours of the forward flow probability. Here (—) are locations with a FFP of 0.5, (- - -) are locations of $y_{\max}$ and $y_{\pm 0.5}$, (—) is the streamline through $x/H_j = 0.05$ and $y/H_j = 1.4$, and (○) and (×) are locations of minimum and maximum curvatures of this streamline.

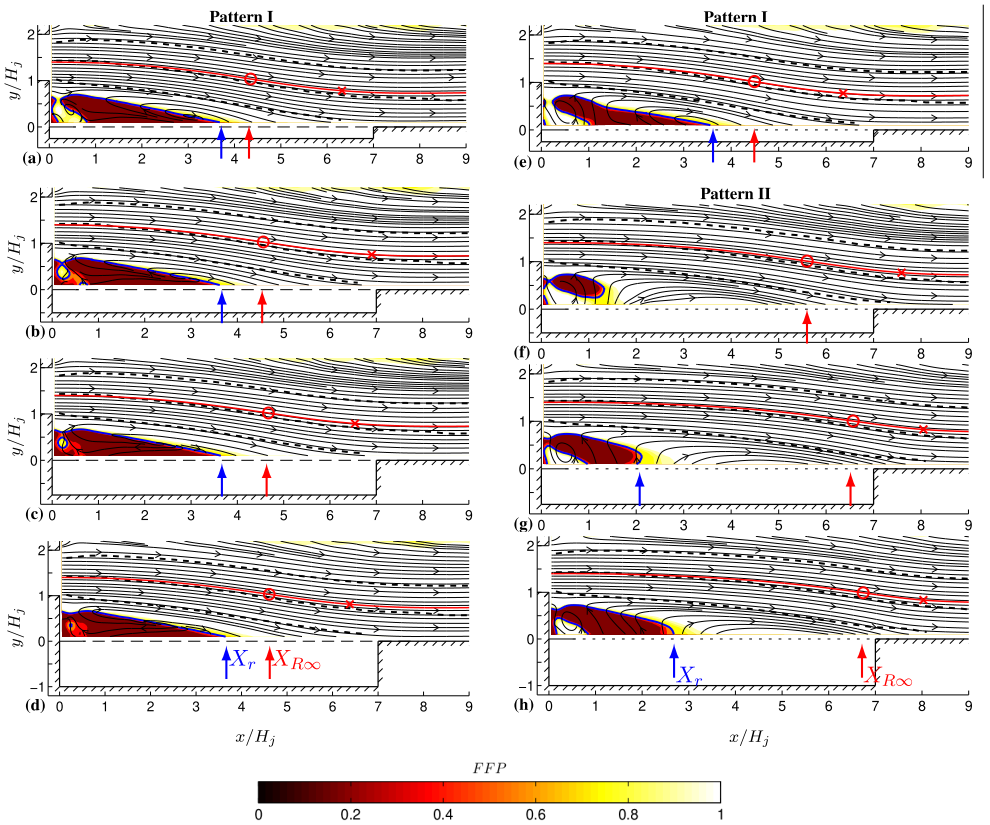

FIG. 6. Streamlines and contours of the FFP for flows over a permeable wall with (a)–(d) $\gamma = 0.1$ and (e)–(h) $\gamma = 0.4$ and cavity depths of (a) and (e) $H_c/H_j = 0.25$, (b) and (f) $H_c/H_j = 0.5$, (c) and (g) $H_c/H_j = 0.75$, and (d) and (h) $H_c/H_j = 1.0$. Other lines and symbols are the same as in Fig. 5.

flow probability was smaller than 0.5 in the lower half of the recirculation region. The time-mean reattachment location $X_{r,o}$, where the FFP was 0.5 at $y/H_j = 0.1$, was $3.8H_j$. This approximately corresponded to the inflection in the curvature of the jet characterized here by the curvature on the streamline approximately corresponding to the maximum velocity in the jet. The curvature on this streamline was zero at $X_{R\infty,o}/H_j \approx 3.9$. The streamline was concave at $x < X_{R\infty,o}$ and was convex at $x > X_{R\infty,o}$ as the jet curved back away from wall after reattachment. The maximum curvature downstream of the reattachment point occurred at $x/H_j \approx 5.5$, marked with a cross ($\times$).

The mean flow field in the jets over the perforated plate showed two different flow patterns, illustrated in Fig. 6 for the perforated walls with open-area ratios γ of 0.1 and 0.4. In the first pattern (referred to as pattern I) for a low open area [Figs. 6(a)–6(d)] or a small cavity depth [Fig. 6(e)], the flow largely recirculated upstream over the perforated bottom wall in a manner similar to the flow over the solid wall. Both the reattachment location X_r and the location of the zero-curvature position $X_{R\infty}$ varied only slightly, suggesting there was only a modest change in the mean flow. In contrast, in the second pattern (referred to as pattern II) for larger open areas and cavity depths [such as $\gamma = 0.4$ and $H_c/H_j \geqslant 0.5$, shown in Figs. 6(f)–6(h)], the presence of the perforated wall had a much larger effect on the jet trajectory with the jet approaching the wall more gradually as the cavity depth increased. Moreover, flow recirculation was not evident over the perforated bottom wall, but appeared to pass downward through the wall near the reattachment point and reenter the separation bubble upward through the wall near the jet outlet, suggesting flow traveled upstream in the cavity. The positions with a FFP of 0.5 in the flows with $H_c/H_j \geqslant 0.75$ were much closer to the

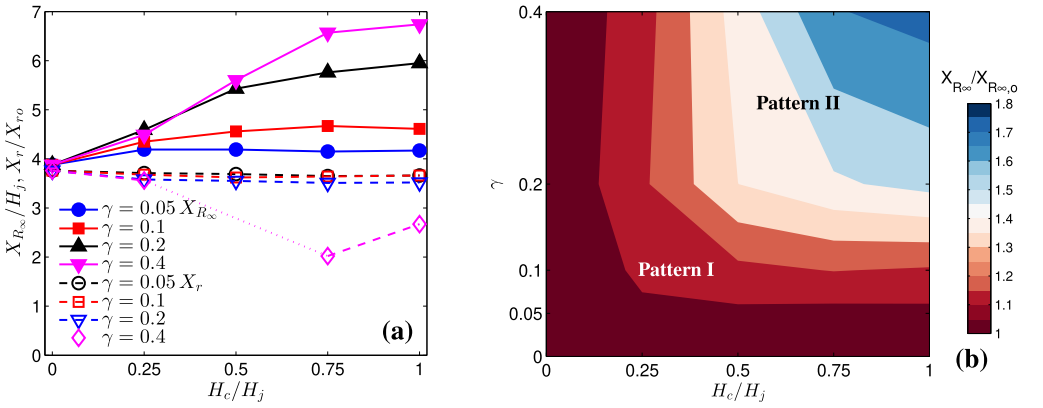

FIG. 7. (a) Change in the streamwise positions of minimum curvature ($R \approx \infty$) on the streamline through $x/H_j = 0.05$ and $y/H_j = 1.4$ ($X_{R\infty}$) and the streamwise positions with a FFP of 0.5 at $y/H = 0.1$ (X_r) with the cavity depths for different open-area ratios. (b) Contours of $X_{R\infty}$ normalized using $X_{R\infty,o}$.

jet exit, shown in Figs. 6(g) and 6(h), and did not appear to reflect the reattachment process of the offset jet that was better reflected by the location of zero streamline curvature near the center of the jet.

The changes in the location of the zero curvature near the center of the jet, $X_{R\infty}$, and the location of 50% FFP, X_r, with cavity depth for the different plates are shown in Fig. 7. The results show that X_r became smaller when a perforated wall was used and decreased as the cavity depth increased in many cases. The zero-curvature position $X_{R\infty}$ increased with the cavity depth in all cases. The increase in $X_{R\infty}$ was modest for flow over plates with small open-area ratios or small cavity depths (pattern I) but became significant when there was evidence of flow through the cavity (pattern II). The static base pressure coefficient $C_P = 2P/\rho U_j^2$ at $x/H_j = 0.25$ showed features similar to those of $X_{R\infty}$, as shown in Fig. 8. A perforated plate of any open-area ratio and any cavity depth caused C_P to increase (became less negative). In pattern I, where the streamline curvature was relaxed slightly, C_P increased only modestly with H_c/H_j. In contrast, C_P increased significantly when the cavity depth increased from $H_c/H_j = 0.25$ to 0.5 in the flows with $\gamma \geqslant 0.2$ where flow transitioned to pattern II. The large increase in C_P was attributed to an increase in flow rate through the cavity. The effects of the cavity depth appeared to be self-limiting in flows with pattern II: Further increasing the

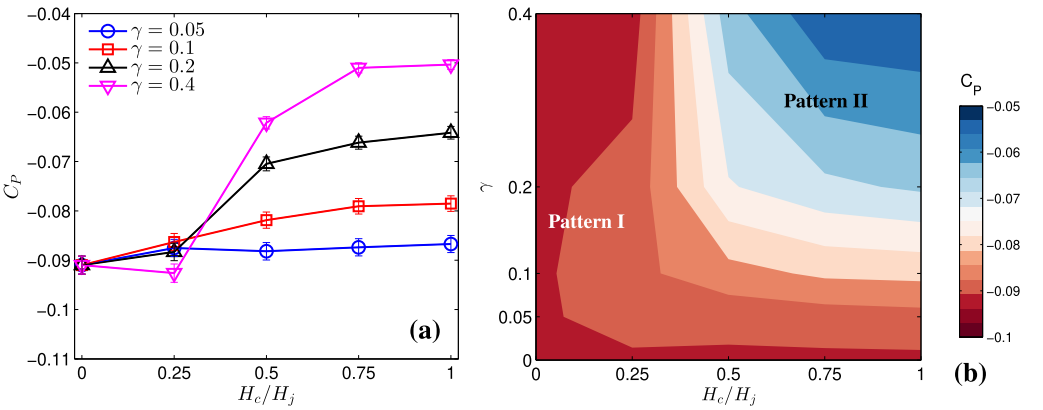

FIG. 8. Change in the static wall pressure coefficients at $x/H = 0.25$ for different open-area ratios γ.

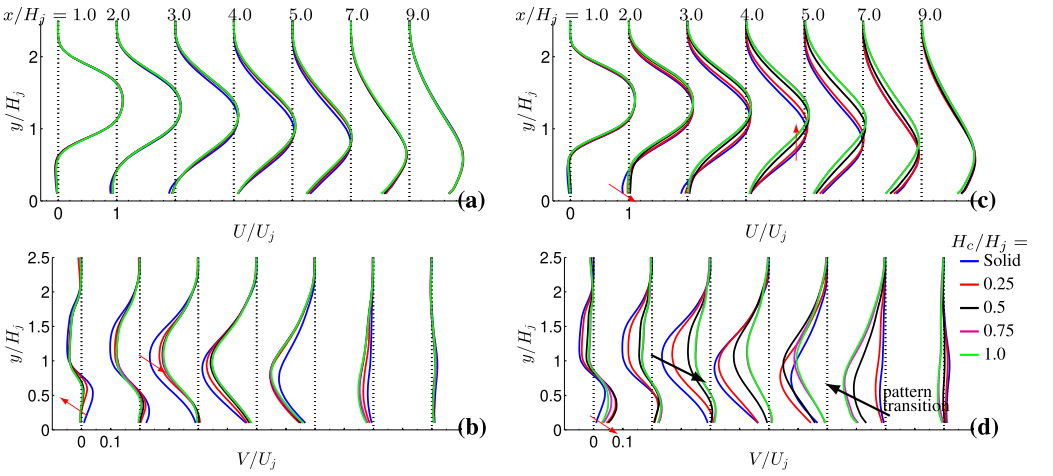

FIG. 9. Profiles of the time-mean streamwise and vertical velocities for flows over (—) a solid bottom wall and permeable walls with (a) and (b) $\gamma = 0.1$ and (c) and (d) $\gamma = 0.4$ for $H_c/H_j = 0.25$ (—), 0.50 (—), 0.75 (—), and 1.0 (—).

cavity depth beyond $H_c/H_j = 0.75$ tended to move $X_{R\infty}$ out of the perforated section [see Fig. 6(h)]. Once out of the perforated section, the attaching jet ceased to further relax due to a decreasing rate of the recirculating flow in the cavity. The critical cavity depth was determined primarily by the position where the perforated section ended, which was $x/H_j = 7.0$ in the present investigation.

The mean streamwise and vertical velocity profiles (U and V) for the flows with $\gamma = 0.1$ and $\gamma = 0.4$ are shown in Fig. 9. In flows of pattern I ($\gamma = 0.1$ and $\gamma = 0.4$ with $H_c/H_j = 0.25$), the

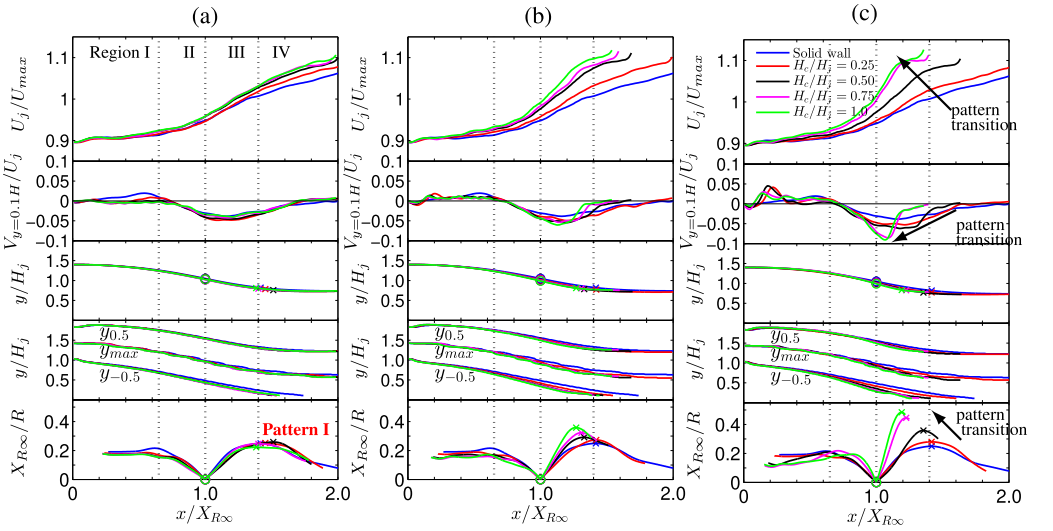

FIG. 10. Change in the maximum local velocity magnitude ($U_j/U_{\max}$), the time-mean vertical velocity at $y/H_j = 0.1$ ($V_{y=0.1H_j}/U_j$), the distance from the wall to the positions of the maximum local velocity and half of the maximum local velocity ($y_{\max}$, $y_{-0.5}$, and $y_{0.5}$) and the streamline through $x/H_j = 0.025$ and $y/H_j = 0.4$ and its curvature ($X_{R\infty}/R$) for flows with (—) a solid and perforated walls with open-area ratios of (a) $\gamma = 0.1$, (b) $\gamma = 0.2$, and (c) $\gamma = 0.4$ for cavity heights of $H_c/H_j = 0.25$ (—), 0.50 (—), 0.75 (—), and 1.0 (—).

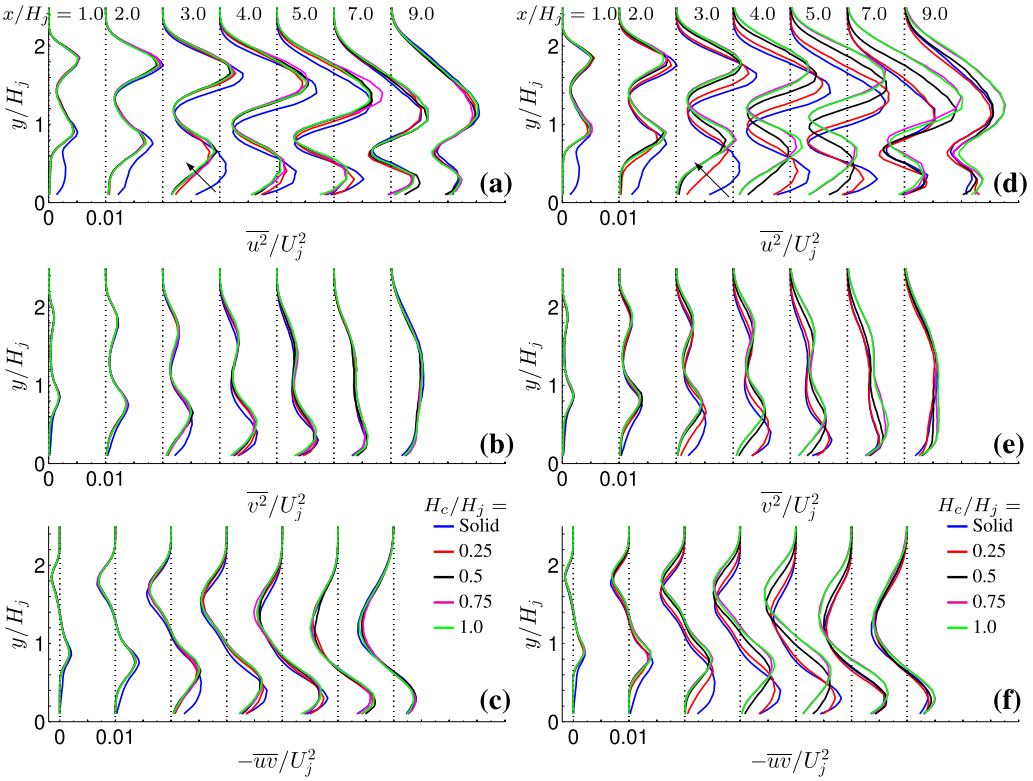

FIG. 11. Profiles of the Reynolds stresses for flows with (—) a solid wall and perforated walls with open-area ratios of (a)–(c) $\gamma = 0.1$ and (d)–(f) $\gamma = 0.4$ and cavity heights $H_c/H_j = 0.25$ (—), 0.50 (—), 0.75 (—), and 1.0 (—).

results show that the presence of the perforated plate and the cavity only had a modest effect on the mean velocity. The presence of the perforated plate slightly reduced the magnitude of both U and V in the recirculation bubble ($x/H_j \leqslant 2.0$) and the jet approached the wall in a more gradual manner as V was less negative at $x/H_j = 3.0$. For flows of pattern II ($\gamma = 0.4$ and $H_c/H_j \geqslant 0.5$), the streamwise velocity U under the jet became nearly zero [$x/H_j = 2$ in Fig. 9(c)], indicating the mean recirculating flow largely disappeared over the bottom wall. The vertical velocity V became much larger near the jet exit [$x/H_j = 1$ in Fig. 9(c)], caused by the upward flow through the cavity and the perforated wall. The jet trajectory became much more gradual as the depth of cavity increased, shown by the increase in V (less negative) at $x/H_j = 3$ in Fig. 9(d) and shift away from the wall of the jet center [$x/H_j = 4$ in Fig. 9(c)].

A comparison of the development of the mean velocity field with the streamwise coordinate x normalized using the zero-curvature length $X_{R\infty}$ is shown in Fig. 10. The trajectories of jets in pattern I deviated slightly from that of the baseline flow. These trajectories largely collapsed and did not vary significantly with the cavity depth H_c [Fig. 10(a)]. The collapsed trajectories, particularly the curvature $X_{R\infty}/R$, suggested that the flow can be divided into several regions with distinct features: Curvature did not change in the region $x/X_{R\infty} \lesssim 0.65$ (region I), decreased quickly to zero at $0.65 \lesssim x/X_{R\infty} \leqslant 1.0$ (region II), increased to a maximum at $1.0 \leqslant x/X_{R\infty} \lesssim 1.4$ (region III), and approached zero at $x/X_{R\infty} \gtrsim 1.4$ (region IV). The division of the attaching jet was similar to that in [13], where X_r was used as the length scale. The Görtler number $(U_j H_j/\nu)(H_j/R)^{1/2}$ was large at the end of regions I and III, where the flow was susceptible to a centrifugal instability [22,34]. Streamline curvatures $X_{R\infty}/R$ of patterns I and II were similar at $x/X_{R\infty} \leqslant 1.0$ [regions I

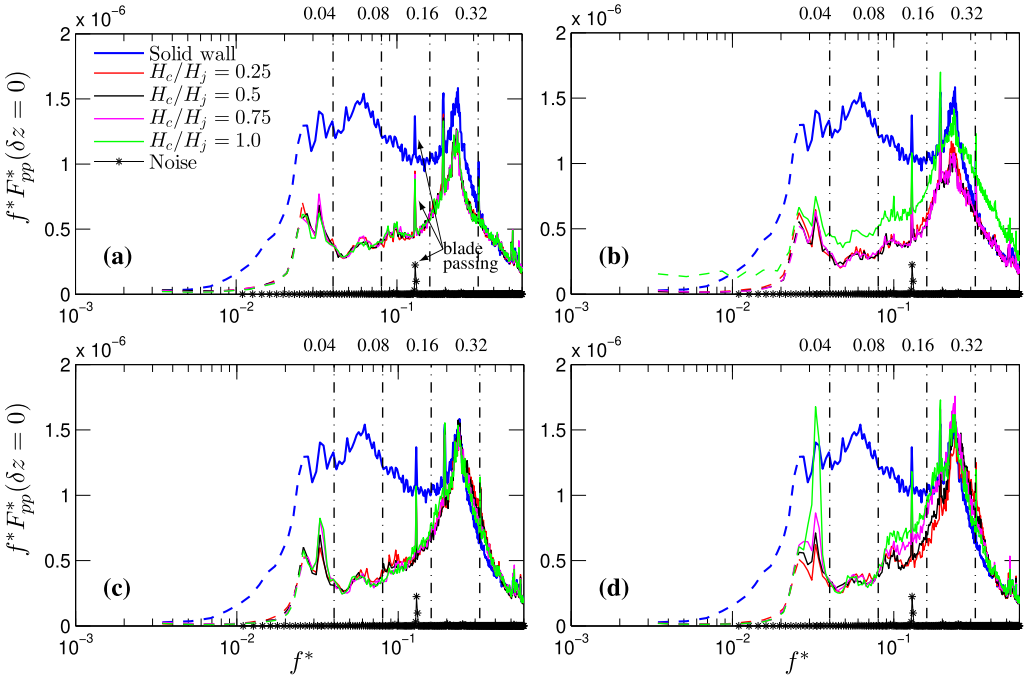

FIG. 12. Premultiplied pressure autospectra, where $f^*F^*_{pp} = fF_{pp}/(0.5\rho U_j^2)^2$ and $f^* = fH_j/U_j$, at $x/H = 0.25$ for the flows over (—) the solid wall and perforated walls with open-area ratios of (a) $\gamma = 0.05$, (b) $\gamma = 0.1$, (c) $\gamma = 0.2$, and (d) $\gamma = 0.4$ and cavity heights $H_c/H_j = 0.25$ (—), 0.50 (—), 0.75 (—), and 1.0 (—). Dashed lines indicate frequencies less than 15 Hz.

and II; see Fig. 10(c)], but became different at $x/X_{R\infty} \geqslant 1.0$ (regions III and IV). At $x/X_{R\infty} \geqslant 1.0$, jets in pattern II curved back parallel to the wall more quickly, resulting in a larger curvature and decrease in the maximum mean velocity in region III. The transition between patterns I and II was

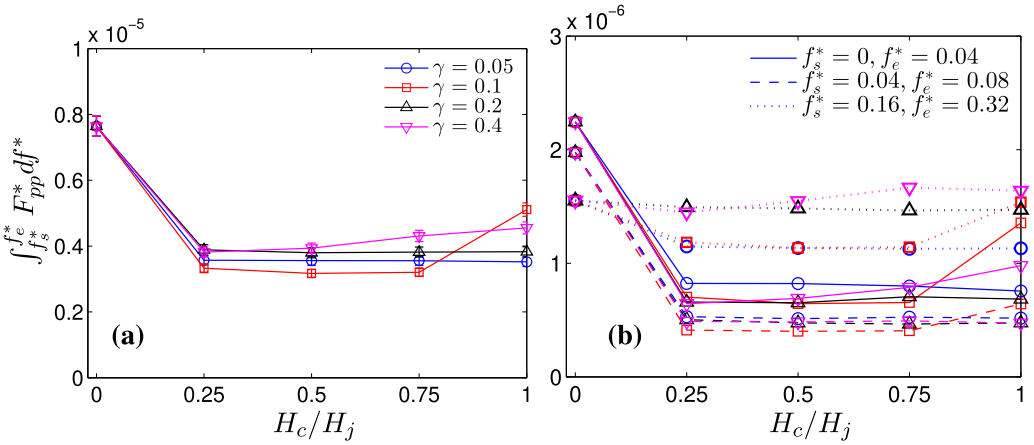

FIG. 13. (a) Change in the integration of the pressure autospectra $\int_{f_s^*}^{f_e^*} F^*_{pp} df^*$ at $x/H = 0.25$ ($f_s^* = 0$ and $f_e^* = \infty$) over the full frequency range $0 < f^* < \infty$ and (b) a frequency band of $f^* \leqslant 0.04$ (—), $0.04 \leqslant f^* \leqslant 0.08$ (—), and $0.16 \leqslant f^* \leqslant 0.32$ (···) for an open-area ratio of $\gamma = 0.05$ (○), $\gamma = 0.1$ (□), $\gamma = 0.2$ (△), and $\gamma = 0.4$ (▽).

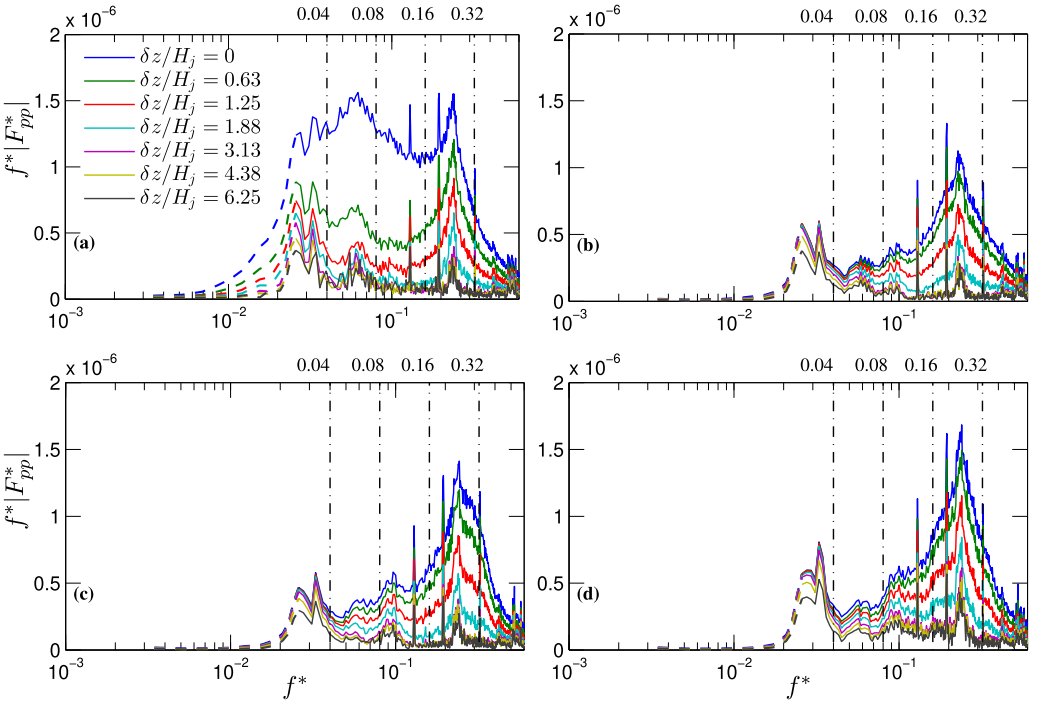

FIG. 14. Premultiplied pressure autospectra and cross spectra, where $f^*|F^*_{pp}| = f|F_{pp}|/(0.5\rho U_j^2)^2$ and $f^* = fH_j/U_j$, at $x/H = 0.25$ for the flows over (a) the solid wall and perforated walls with (b) $\gamma = 0.1$ and $H_c/H_j = 0.25$, (c) $\gamma = 0.2$ and $H_c/H_j = 0.25$, and (d) $\gamma = 0.4$ and $H_c/H_j = 0.75$ for $\delta z = 0$ (—), 0.63 (—), 1.25 (—), 1.88 (—), 3.13 (—), 4.38 (—), and 6.25 (—).

characterized by an increase in the magnitude of the mean vertical velocity near the wall in region III and near the jet outlet as noted previously. The effect of the finite cavity length on the development of the flow was evident for the case with $\gamma = 0.4$.

B. Fluctuations

Distributions of the Reynolds stresses in the flows over the wall with $\gamma = 0.1$ and 0.4 are shown in Fig. 11. The results in both cases show a region of elevated Reynolds stresses in the inner and outer shear layers of the attaching jet, similar to the results for offset jet flows over solid walls with small offset distances in [13,28]. The presence of the perforated plate significantly reduced the Reynolds stresses in the recirculating region between the jet and the perforated wall, even in the flow with a plate of the smallest open area and the smallest cavity depth. The decrease in Reynolds stresses was particularly evident in the near-wall region of the $\overline{u^2}$ profiles [see Figs. 11(a) and 11(d)] throughout the region.

The normalized spectra of the fluctuating wall pressure $F^*_{pp} = F_{pp}(U_j/H_j)/(0.5\rho U_j^2)^2$ measured at $x/H = 0.25$ for the flow with a solid wall and perforated walls are compared in Fig. 12. The spectra are premultiplied by f^* so that the relative area under the curve in each band reflects the relative energy in that band. The ambient noise level measured for the flow over the solid wall was much smaller than the wall pressure signal in all cases except at the blade passage frequencies. The spectrum for the flow over a solid wall was similar to those in [13,14]. There was evidence of upstream propagation of wall pressure fluctuations below an offset jet over a solid wall for $f^* \lesssim 0.11$ in [14] and downstream propagation only for $f^* > 0.16$. The upstream propagation velocity increased in proportion to the frequency for $f^* < 0.04$, was approximately

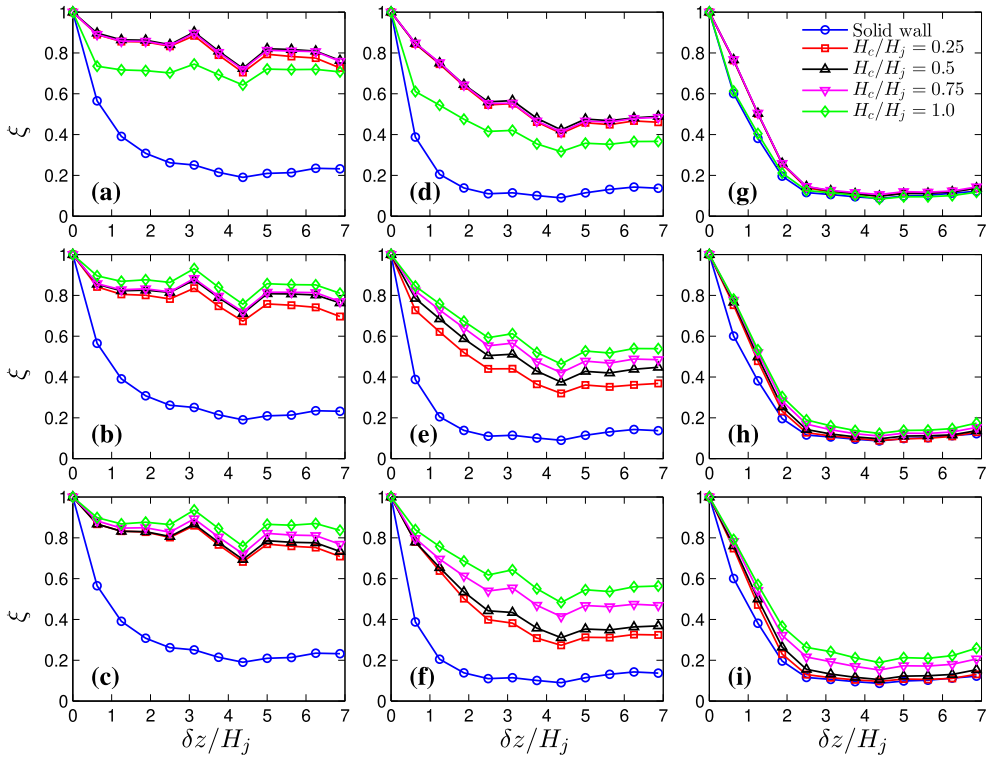

FIG. 15. Changes in the integration of the magnitude of the cross spectra over the frequency range $f_s^* \leqslant f^* \leqslant f_e^*$, normalized using the integration of the autospectra $\xi = \int_{f_s^*}^{f_e^*} |F_{pp}^*(\delta z)| df^* / \int_{f_s^*}^{f_e^*} F_{pp}^*(\delta z = 0) df^*$, for pressure fluctuations at $x/H_j = 0.25$ in frequency ranges (a)–(c) $f_s^* = 0$ and $f_e^* = 0.04$, (d)–(f) $f_s^* = 0.04$ and $f_e^* = 0.08$, and (g)–(i) $f_s^* = 0.16$ and $f_e^* = 0.32$ for flows over a solid wall and perforated walls with open-area ratios of (a), (d), and (g) $\gamma = 0.1$; (b), (e), and (h) $\gamma = 0.2$; and (c), (f), and (i) $\gamma = 0.4$.

constant for $f^* \sim 0.06$–0.08, and increased again with frequency above this range, suggesting that different motions or modes were present [14]. The proportional change for $f^* < 0.04$ combined with a similar behavior in the downstream propagation velocity in the reattachment region was attributed to the flapping of the recirculation region in [14]. The largest coherence in this range occurs at $f^* \sim 0.01$ in [14]. The results here show that the presence of the perforated wall significantly attenuated pressure fluctuations with $f^* \lesssim 0.16$ but had only a small effect on the pressure fluctuations with $0.16 \lesssim f^* \lesssim 0.32$. The attenuation was particularly large for $f^* \lesssim 0.08$.

The change in the pressure fluctuations at $x/H = 0.25$ with the cavity depth was evaluated by integrating the autospectra over the full frequency range and the results of the integrations, shown in Fig. 13(a), are the mean-square value of the fluctuating wall pressure $\overline{p^2}/(0.5\rho U_j^2)^2 = \int_0^\infty F_{pp}^* df^*$. The presence of the perforate plate reduced the mean-square value by approximately 50%. The results suggest that the effect of varying the open-area ratio or the cavity depth on the fluctuating pressure at this location was small. The changes in the fluctuations associated with different frequency ranges were evaluated by integrating the spectra over different frequency bands and the results are shown in Fig. 13(b). The attenuation of the fluctuations was large in the low-frequency bands $f^* \leqslant 0.08$, whereas fluctuation of $0.16 \leqslant f^* \leqslant 0.32$ only changed modestly.

The three-dimensional nature of the fluctuations at $x/H_j = 0.25$ was studied by comparing the autospectra with the magnitude of the cross spectra, shown in Fig. 14. In the flow with a solid wall [Fig. 14(a)] the magnitude of the cross spectra decreased significantly as distance δz increased.

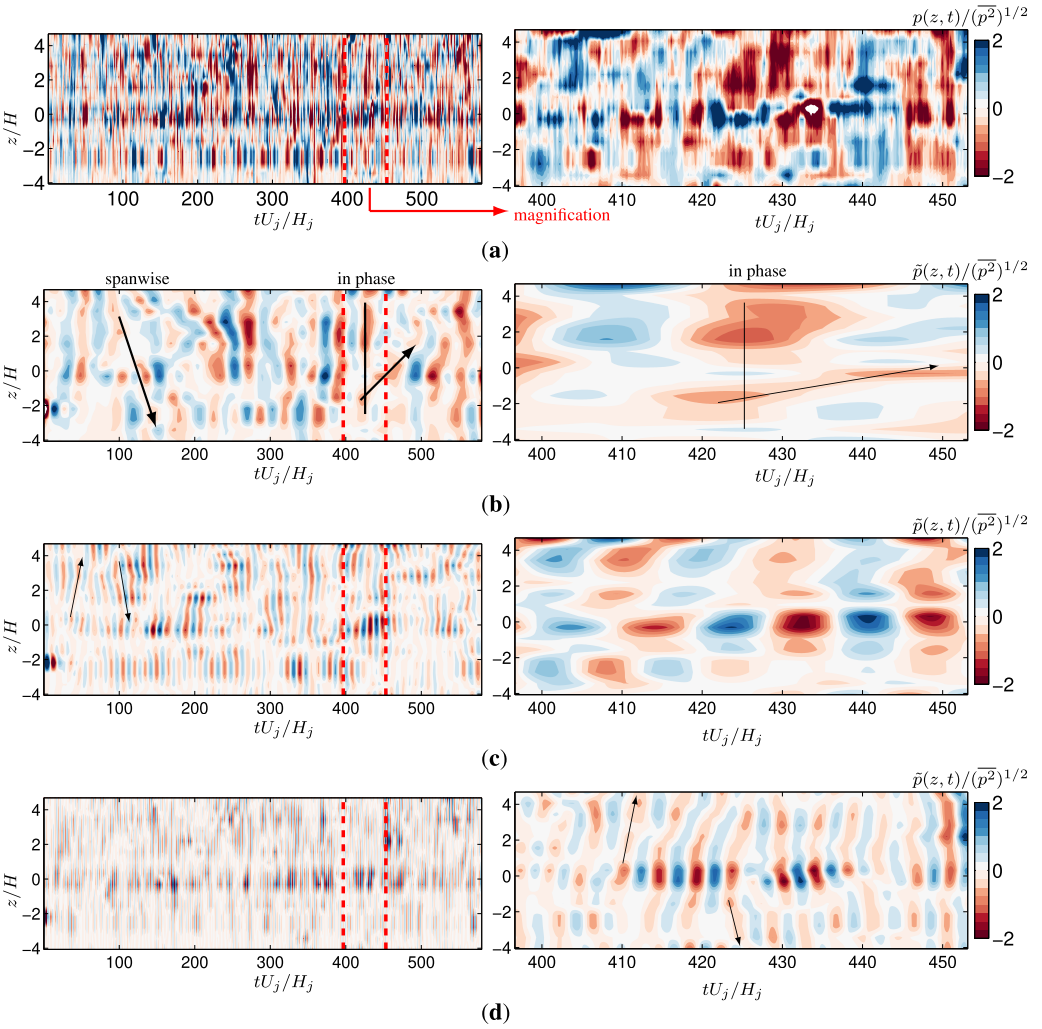

FIG. 16. Typical transient of the fluctuating pressure at $x/H_j = 0.25$ for the flow with a solid wall for (a) the unfiltered full signal p and (b)–(d) the filtered signals for frequency ranges (b) $f^* \leqslant 0.04$, (c) $0.04 \leqslant f^* \leqslant 0.08$, and (d) $0.16 \leqslant f^* \leqslant 0.32$. Transient pressure was normalized using the root-mean-square value of the full signal $(\overline{p^2})^{1/2}$.

The decrease rate became modest when δz was larger than $1.88H_j$. In the flows with a perforated wall [see, e.g., Figs. 14(b)–14(d)], the magnitude of the cross spectra changed moderately in the frequency range $0.026 \lesssim f^* \lesssim 0.04$ but decreased significantly in the ranges $0.04 \lesssim f^* \lesssim 0.08$ and $0.16 \lesssim f^* \lesssim 0.32$. In all flows, including the one with a solid wall and those with perforated walls, the magnitudes of the cross spectra were similar when $\delta z/H_j$ was larger than 1.88.

The three-dimensional nature of the fluctuations in different ranges was further characterized by integrating the magnitude of the cross spectra in different frequency ranges, shown in Fig. 15. The results of the integrations were normalized using the integration of the corresponding autospectra over the same frequency range and represented the spanwise correlations of the pressure fluctuations. The results show a significant increase in the spanwise correlation of the pressure with $f^* \leqslant 0.08$ [Figs. 15(a)–15(f)] when the perforated plate was present, indicating a significant decrease in

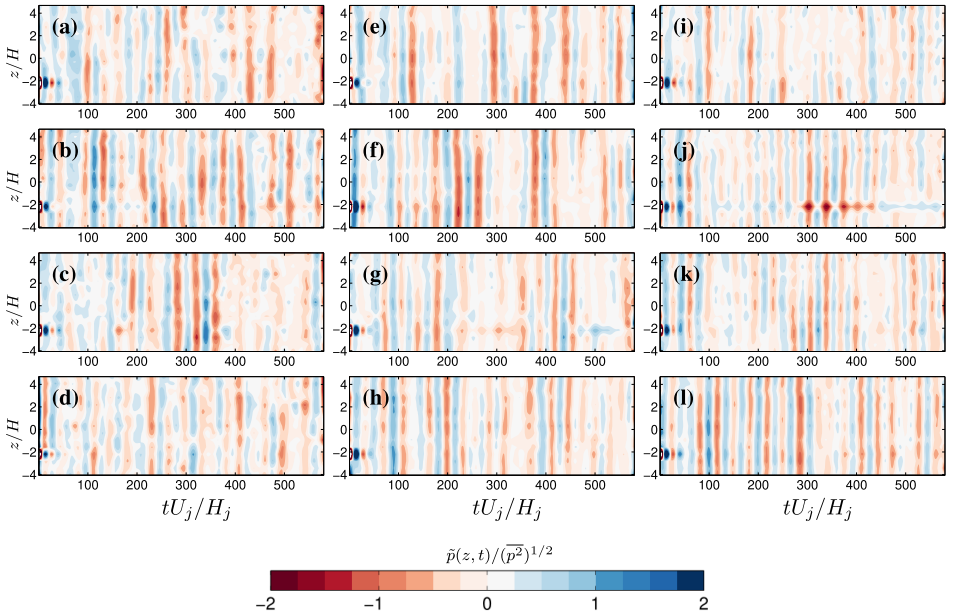

FIG. 17. Typical transients of the pressure for the frequency range $f^* \leqslant 0.04$ for flows over the perforated walls, normalized by using the root-mean-square value of the full signal $(\overline{p^2})^{1/2}$ with cavity depths (a), (e), and (i) $H_c/H_j = 0.25$; (b), (f), and (j) $H_c/H_j = 0.5$; (c), (g), and (k) $H_c/H_j = 0.75$; and (d), (h), and (l) $H_c/H_j = 1.0$ and open-area ratios of (a)–(d) $\gamma = 0.05$, (e)–(h) $\gamma = 0.1$, and (i)–(l) $\gamma = 0.4$.

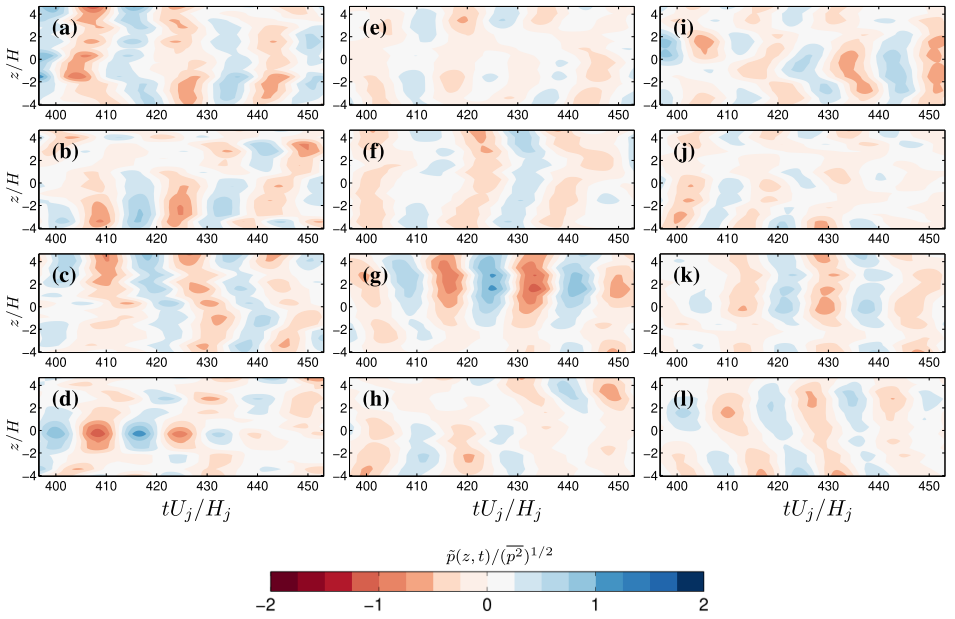

FIG. 18. Typical transients of the pressure for the frequency range $0.04 \leqslant f^* \leqslant 0.08$ for flows over the perforated walls, normalized using the root-mean-square value of the full signal with cavity depths (a), (e), and (i) $H_c/H_j = 0.25$; (b), (f), and (j) $H_c/H_j = 0.5$; (c), (g), and (k) $H_c/H_j = 0.75$; and (d), (h), and (l) $H_c/H_j = 1.0$ and open-area ratios of (a)–(d) $\gamma = 0.05$, (e)–(h) $\gamma = 0.1$, and (i)–(l) $\gamma = 0.4$.

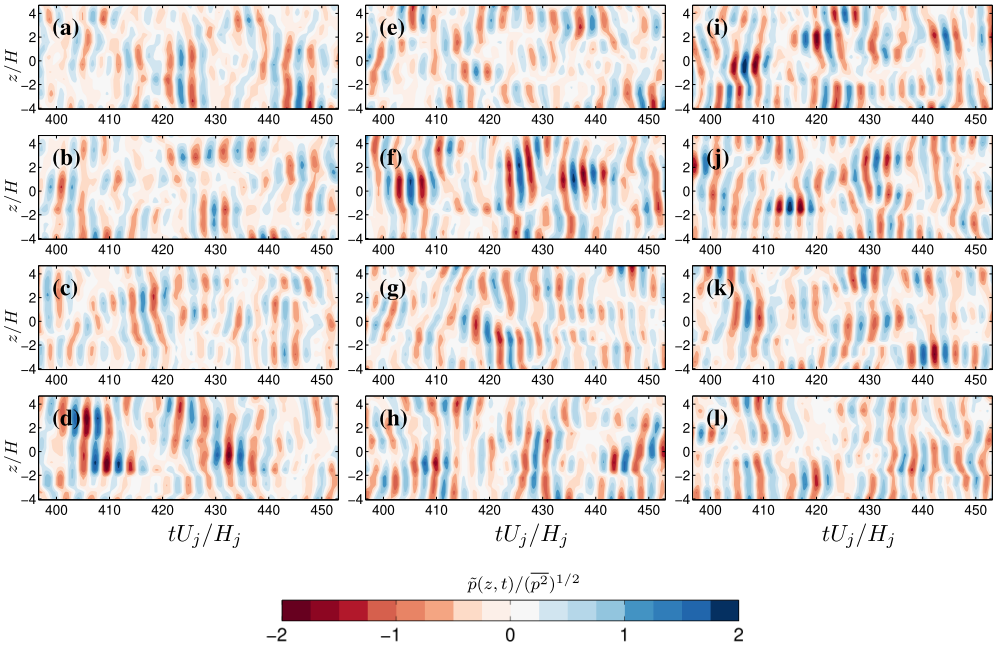

FIG. 19. Typical transients of the pressure for the frequency range $0.16 \leqslant f^* \leqslant 0.32$ for flows over the perforated walls, normalized using the root-mean-square value of the full signal with cavity depths (a), (e), and (i) $H_c/H_j = 0.25$; (b), (f), and (j) $H_c/H_j = 0.5$; (c), (g), and (k) $H_c/H_j = 0.75$; and (d), (h), and (l) $H_c/H_j = 1.0$ and open-area ratios of (a)–(d) $\gamma = 0.05$, (e)–(h) $\gamma = 0.1$, and (i)–(l) $\gamma = 0.4$.

the three-dimensionality. In contrast, there were only modest increases in the three-dimensionality of the higher-frequency fluctuations, as shown in Figs. 15(g)–15(i).

The three-dimensional nature of flows was further examined using the transients of unfiltered pressure across the flow at $x/H_j = 0.25$, with the passing bands of $f^* \leqslant 0.04$, $0.04 < f^* \leqslant 0.08$, and $0.16 < f^* \leqslant 0.32$. Typical results for the flow over the solid wall are shown in Fig. 16. There were three-dimensional features in all three frequency ranges as highlighted in Figs. 16(b)–16(d): with fluctuations in phase across the flow and fluctuations with variations across the flow that appear to be aligned at both positive and negative angles relative to the flow direction without a preference.

The transients of the filtered pressure $\tilde{p}/(\overline{p^2})^{1/2}$ associated with the three frequency ranges are shown in Fig. 17–19, respectively. The results show that the fluctuations with $f^* \leqslant 0.08$ (see Figs. 17 and 18) were largely in phase in the spanwise direction. Thus, the measurements suggest that the perforated plate was effective in attenuating the three-dimensional fluctuations in the base pressure for $f^* < 0.08$, but not effective for the more two-dimensional motions in this frequency range. In contrast, there were only modest changes in the transients of $0.16 \leqslant f^* \leqslant 0.32$ (see Fig. 19).

IV. CONCLUSION

The development of a turbulent offset attaching jet with a small offset distance ($H_s = H_j$) changed significantly when a portion of the wall below the attaching jet was replaced with a perforated plate and a closed cavity underneath the perforated section. Both parameters, open-area ratio and cavity depth, had a large impact on the flow. Two distinct mean flow patterns were observed for different open-area ratios and cavity depths. In the flows with either a small open-area ratio or a small cavity depth, recirculation occurred primarily above the bottom wall.

There were only modest changes in the jet curvature and the static base pressure. In the flows with a large open-area ratio and a large cavity depth, flow recirculated primarily under the perforated wall and upward into the separation bubble near the jet exit. As a result, the jet curvature and the static base pressure changed significantly.

The presence of the perforated plate resulted in an attenuation in the Reynolds stresses in the region between the jet and the wall and the fluctuating base wall pressure in all cases even when the presence of the perforated plate had only a small effect on the development of the offset jet and the recirculating flow below the jet. The impact of the perforated wall differed for different frequencies. The presence of the plate attenuated the spanwise varying fluctuations with $f^* \lesssim 0.08$. Upstream propagation of the pressure fluctuations was reported for this range by Gao and Ewing [14] for an offset jet flow over the solid wall. There appeared to be less damping of the fluctuations that were largely in phase across the flow in this range. The presence of the perforated plate had little effect on the fluctuations with $0.16 \lesssim f^* \lesssim 0.32$. The measurements by Gao and Ewing [14] suggest there was only downstream propagation of the pressure fluctuations in this range.

ACKNOWLEDGMENT

This work was supported by National Natural Science Foundation of China through Grants No. 11572078 and No. 91752101.

[1] R. L Simpson, Turbulent boundary-layer separation, Annu. Rev. Fluid Mech. **21**, 205 (1989).
[2] L. Chen, K. Asai, T. Nonomura, G. Xi, and T. Liu, A review of backward-facing step (BFS) flow mechanisms, heat transfer and control, Therm. Sci. Eng. Prog. **6**, 194 (2018).
[3] M. A. Z. Hasan, The flow over a backward-facing step under controlled perturbation: Laminar separation, J. Fluid Mech. **238**, 73 (1992).
[4] D. M. Driver, H. L. Seegmiller, and J. G. Marvin, Time-dependent behavior of a reattaching shear layer, AIAA J. **25**, 914 (1987).
[5] A. F. Heenan and J. F. Morrison, Passive control of pressure fluctuations generated by separated flow, AIAA J. **36**, 1014 (1998).
[6] A. F. Heenan and J. F. Morrison, Passive control of backstep flow, Exp. Therm. Fluid Sci. **16**, 122 (1998).
[7] Y. Z. Liu, W. Kang, and H. J. Sung, Assessment of the organization of a turbulent separated and reattaching flow by measuring wall pressure fluctuations, Exp. Fluids **38**, 485 (2005).
[8] I. Lee and J. Sung, Multiple-arrayed pressure measurement for investigation of the unsteady flow structure of a reattaching shear layer, J. Fluid Mech. **463**, 377 (2002).
[9] L. M. Hudy, A. M. Naguib, and W. M. Humphreys, Stochastic estimation of a separated-flow field using wall-pressure-array measurements, Phys. Fluids **19**, 024103 (2007).
[10] A. S. Neto, D. Grand, O. Métais, and M. Lesieur, A numerical investigation of the coherent vortices in turbulence behind a backward-facing step, J. Fluid Mech. **256**, 1 (1993).
[11] H. Le, P. Moin, and J. Kim, Direct numerical simulation of turbulent flow over a backward-facing step, J. Fluid Mech. **330**, 349 (1997).
[12] P. G. Spazzini, G. Iuso, M. Onorato, N. Zurlo, and G. M. Di Cicca, Unsteady behavior of back-facing step flow, Exp. Fluids **30**, 551 (2001).
[13] N. Gao and D. Ewing, Experimental investigation of planar offset attaching jets with small offset distances, Exp. Fluids **42**, 941 (2007).
[14] N. Gao and D. Ewing, On the phase velocities of the motions in an offset attaching planar jet, J. Turbul. **9**, N27 (2008).
[15] M. Kiya and K. Sasaki, Structure of a turbulent separation bubble, J. Fluid Mech. **137**, 83 (1983).
[16] I. P. Castro and A. Haque, The structure of a turbulent shear layer bounding a separation region, J. Fluid Mech. **179**, 439 (1987).

[17] N. J. Cherry, R. Hillier, and M. Latour, Unsteady measurements in a separated and reattaching flow, J. Fluid Mech. **144**, 13 (1984).
[18] D. Wee, T. Yi, A. Annaswamy, and A. F. Ghoniem, Self-sustained oscillations and vortex shedding in backward-facing step flows: Simulation and linear instability analysis, Phys. Fluids **16**, 3361 (2004).
[19] J. K. Eaton and J. P. Johnson, in *Turbulent Shear Flows 3: Selected Papers from the Third International Symposium on Turbulent Shear Flows, The University of California, Davis, 1981*, edited by L. J. S. Bradbury, F. Durst, B. E. Launder, and F. W. Schmidt (Springer, Berlin, 1982), pp. 162–170.
[20] V. Statnikov, I. Bolgar, S. Scharnowski, M. Meinke, C. J. Kähler, and W. Schröder, Analysis of characteristic wake flow modes on a generic transonic backward-facing step configuration, Eur. J. Mech. B **59**, 124 (2016).
[21] S. Scharnowski, I. Bolgar, and C. J. Kähler, Characterization of turbulent structures in a transonic backward-facing step flow, Flow Turbul. Combust. **98**, 947 (2017).
[22] J. F. Beaudoin, O. Cadot, J. L. Aider, and J. E. Wesfreid, Three-dimensional stationary flow over a backward-facing step, Eur. J. Mech. B **23**, 147 (2004).
[23] D. Barkley, M. Gomes, and R. D. Henderson, Three-dimensional instability in flow over a backward-facing step, J. Fluid Mech. **473**, 167 (2002).
[24] D. Lanzerstorfer and H. C. Kuhlmann, Global stability of the two-dimensional flow over a backward-facing step, J. Fluid Mech. **693**, 1 (2012).
[25] K. B. Chun and H. J. Sung, Control of turbulent separated flow over backward-facing step by local forcing, Exp. Fluids **21**, 417 (1996).
[26] N. Benard, P. Sujar-Garrido, J. P. Bonnet, and E. Moreau, Control of the coherent structure dynamics downstream of a backward facing step by DBD plasma actuator, Int. J. Heat Fluid Flow **61**, 158 (2016).
[27] V. Uruba, P. Jonáš, and O. Mazur, Control of a channel-flow behind a backward-facing step by suction/blowing, Int. J. Heat Fluid Flow **28**, 665 (2007).
[28] A. Nasr and J. C. S. Lai, Comparison of flow characteristics in the near field of two parallel plane jets and an offset plane jet, Phys. Fluids **9**, 2919 (1997).
[29] N. Gao and D. Ewing, in *Proceedings of the 49th AIAA Aerospace Sciences Meeting including the New Horizons Forum and Aerospace Exposition, Orlando, 2011* (AIAA, Reston, 2011), paper 2011–43.
[30] M. Raffel, C. E. Willert, S. T. Wereley, and J. Kompenhans, *Particle Image Velocimetry: A Practical Guide*, 2nd ed. (Springer, Berlin, 2007).
[31] B. Wieneke, PIV uncertainty quantification from correlation statistics, Meas. Sci. Technol. **26**, 074002 (2015).
[32] J. S. Bendat and A. G. Piersal, *Engineering Application of Correlation and Spectral Analysis*, 2nd ed. (Wiley, New York, 1993), pp. 71–72.
[33] V. Pratt, Direct least-squares fitting of algebraic surfaces, Comput. Graph. **21**, 145 (1987).
[34] H. Görtler, On the three-dimensional instability of laminar boundary layers on concave walls, NACA Report No. 1375, 1954 (unpublished).